Analysis of differential infrared thermography for boundary layer transition detection

A.D. Gardner · C. Eder · C. C. Wolf · M.Raffel

Abstract This paper presents an analysis of the differential infrared thermography (DIT) technique, a contactless method of measuring the unsteady movement of the boundary layer transition position on an unprepared surface. DIT has been shown to measure boundary layer positions which correlate well with those from other measurement methods, and in this paper unsteady aerodynamics from a 2D URANS solution are used and the resulting wall temperatures computed. The results show that only the DIT peak can be analysed, but that this correlates well with the boundary layer transition position. A small systematic time-lag of 1.5 ms cannot be reduced by using different surface materials, but the signal can be improved by using common plastics as a thin sheet on the surface.

A.D. Gardner
German Aerospace Center (DLR)
Institute of Aerodynamics and Flow Technology,
Bunsenstrasse 10,
37073 Göttingen,
Germany.
E-mail: Tony.Gardner@dlr.de

C. Eder
Bundeswehr University Munich
Department of Mechanical Engineering,
85577 Neubiberg
Germany.

C. C. Wolf
German Aerospace Center (DLR)
E-mail: Christian.Wolf@dlr.de

M. Raffel
German Aerospace Center (DLR)
E-mail: Markus.Raffel@dlr.de

Nomenclature

α	Instantaneous angle of attack (°)
α_0	Mean angle of attack (°)
α_1	Pitching amplitude (°)
a_d	Thermal diffusivity (m^2/s)
c	Airfoil chord length (m)
C_f	Skin friction coefficient
C_p	Pressure coefficient
σC_p	Standard deviation in C_P
C	Specific heat capacity (J/kg/K)
ΔT	Temperature difference between two times (K)
ε	Emissivity
f	Pitching frequency (Hz)
f_0	Focal length (m)
ft	Normalised period time
H_L	Lamp heat flux (W/m^2)
kv	Thermal conductivity vertically (W/m/K)
kh	Thermal conductivity horizontally W/m/K)
M	Mach number
n	Boundary value for the transition code
$\dot{q}$	Heat flux (W)
ρ	density (kg/m^3)
Re	Reynolds number
t	Time (s)
T	Wall temperature (K)
T_r	Flow recovery temperature (K)
Tu	Freestream turbulence level
v	Local flow velocity (m/s)
x	Coordinate in the flow direction (m)
y	Coordinate in breadth (m)
z	Coordinate in depth (vertical) (m)

1 Introduction

Unsteady boundary layer transition is an important phenomenon, having an effect on the efficiency and stall point of helicopter main rotor blades (Heister, 2013; Richter and Schülein, 2014; Raffel et al., 2011), Wind turbines (Du and Selig, 2000; Langtry et al., 2006; Lanzafame et al., 2013) and propellers (Schülein, 2014). Many of the classical methods of detecting steady boundary layer transition, including china clay/sublimation (Richards and Burstall, 1945; Velkoff et al., 1971) or microphones (Døssing , 2008) do not work for unsteady flows. Other methods, including hot-film anemometry (Schultz and Jones, 1973) or the σC_p method of pressure analysis (Gardner and Richter, 2015) require the installation of finely discretised sensor arrays and significant data analysis. Hot-wire or Pitot boundary layer measurements (Nitsche and Brunn, 2006) could also be used for unsteady flows, but are impractical for moving surfaces. In contrast, differential infrared thermography offers a contactless method of measuring the unsteady boundary layer transition without surface preparation for nonmetallic surfaces.

Infrared cameras have long been used for flow analysis, with the observations of Thomann and Frisk (1967) being the first published experiments. For a long time the only applications were in hypersonic research due to the low sensitivity of the cameras available (Gartenberg and Roberts, 1992). The first subsonic investigations by Bouchardy et al. (1983) used a measurement of the recovery temperature in transonic flow to measure boundary layer transition. The work of Quast (1987) extended the application range by using a heated wall to measure heat transfer rather than recovery temperature, thus significantly increasing the signal available for measurement. Quast measured boundary layer transition and the laminar separation bubble at the boundary between laminar and turbulent boundary layer flow. The wall can be directly heated by thin films (Astarita and Cardone, 2000), or indirectly using infrared lamps (Raffel and Merz, 2014). An overview of some recent experiments separation and transition detection using these methods is given by Carlomagno and Cardone (2010). With the availability on the market of high-speed infrared cameras, they have been used for the detection of boundary layer transition in the rotating system where that would not previously have been possible due to the camera framing time, including on a helicopter hovering in ground effect (Richter and Schülein, 2014).

Differential infrared thermography (DIT) is a new optical measurement technique based on infrared thermography suggested by Raffel and Merz (2014) for the unsteady boundary layer transition detection on pitching rotor blade airfoils. It has since been shown to work for boundary layer transition detection on rotating blades Raffel et al. (2015) and a variant of the method has been shown to detect dy-
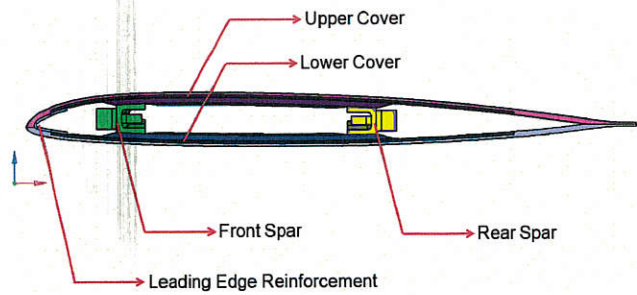

Fig. 1 Cut through the airfoil showing the shell design, from Uenal and Grieb (2013).

namic stall Gardner et al. (2016). The technique is based on the difference between two thermal measurement images and analyzes differences in the surface temperatures existing between regions of laminar and turbulent flow in order to determine a moving boundary layer transition location.

This paper uses skin friction distributions from 2D steady and unsteady computations to produce computed DIT results. These can be used to show that DIT can be used to compute a mean boundary layer transition position (with a small systematic error), but not generally the start and end of the boundary layer transition region.

2 Experiment for DIT

The experiment for DIT which is computed in this paper was reported by Richter et al. (2016), and a summary is presented here. A 2D airfoil was installed in 1 m x 1 m adaptive-wall test section of the Transonic Wind tunnel Göttingen (TWG) with the 9% airfoil DSA-9A. The chord length was 300 mm and the airfoil spanned the whole width of the wind tunnel with small gaps of 1.5 mm between the airfoil ends and the wind tunnel wall. The airfoil was pitched using drive shafts at the c/4 position which extended through the wind tunnel walls. For the test case presented here, the flow had M=0.30, Re=1.8×10^6 and the pitching was sinusoidal at f=6.6 Hz with an amplitude of α_1=±6° around the mean angle of attack of α_0=5° for a movement of $\alpha = 5 + 6sin(2\pi5.5t)$.

The airfoil was constructed using carbon-fibre-shells (Fig. 1), and was instrumented with Kulite pressure sensors directly under the shell surface and hot-film gauges. The hot-film gauges can be analysed to give boundary layer transition position, and the pressure sensors were also used to detect the boundary layer transition position using the σC_P method of Gardner and Richter (2015) for periodic flows.

The optical setup is shown in Fig. 2, where the surface of the airfoil is warmed by a 2 kW lamp and the infrared emission of the surface is monitored by a high-speed infrared camera (FLIR SC7750-L) at 190 Hz. The high-speed infrared camera had a spectral range of 8.0-9.4 μm detected by a Cadmium-Mercury-Telluride FPA-detector. An $f_0 = 50$ mm lens with an aperture f_0 /2.0 was used. The data acquisition

was performed with an integration time of $100\,\mu s$, with a reduced detector region of $640 \times 310\,\mathrm{px}^2$ and with an acquisition rate of f = 190 Hz. The DIT method evaluates intensity differences in the thermal images, it is not dependent on a calibration of the absolute temperature, but a temperatures are computed for comparison with the computation. The output of the camera was monitored with the data acquisition system for the pressure and angle of attack sensors so that a synchronization between the different systems could be achieved. The camera has a noise equivalent temperature difference (NETD) of <18 mK and images were acquired using the "Altair" software. An example image is shown in Fig. 3.

The surface properties of the airfoil have a significant effect on the infrared signal measured, as recently explored by Simon et al. (2016). The airfoil surface was made of carbon-fibre reinforced plastic with a black colour, with an estimated emissivity of $\varepsilon = 0.95$ (Richter et al., 2016). An external layer of unreinforced resin was painted into the mould during manufacture, and this layer was polished after the airfoil was removed from the mould. The airfoil is made of two 3 mm shells (top and bottom) constructed using the L285/H287 system of the firm Hexion. The mid-part of the airfoil is reinforced with a 1.5 mm spar (Fig. 1), for a total thickness of 5.5 mm. For the computations the thickness of 5.5 mm was used, however as will be seen later, the variable thickness of the surface shell due to the spar is not important for the computation of the surface temperatures. The fibre volume of the carbon-fibre shells is 45%. We do not have exact values for the thermal properties of the surface, but from the material data sheets of the epoxy and carbon fibre weaves estimate the thermal conductivity through the shell as $kv = 0.5$ W/m/K and along the shell as $kh = 7$ W/m/K, density $\rho = 1180$ kg/m^3 and specific heat capacity $C = 2300$ J/kg/K. Thus, the surface has low heat conductivity in the vertical direction.

3 Differential infrared thermography

The basis of DIT is a heated model surface which establishes a temperature difference between the surface and the flow. this results in a heat transfer from the model into the flow, cooling the airfoil surface. Due to the difference in the heat exchange rate between laminar and turbulent flows, lower surface temperatures are produced by turbulent flow than by laminar flow.

The original paper DIT of Raffel and Merz (2014) assumed that the temperature distributions for a heated airfoil are purely a function of the local heat flux, which gives the distributions of C_f (or Stanton number), see Fig. 4. The assumptions (for boundary layer transition moving upstream) were:
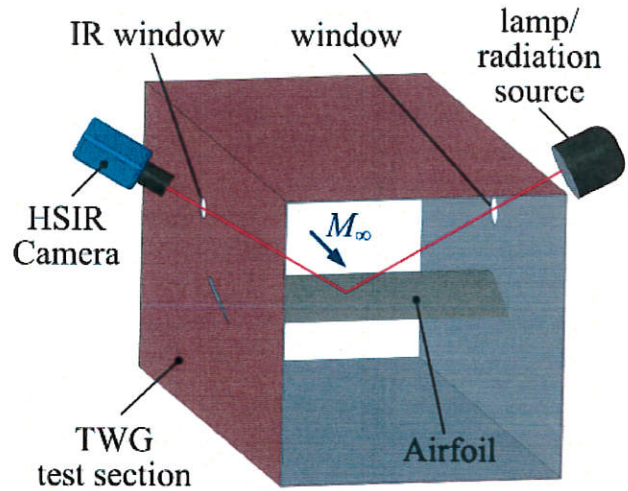

Fig. 2 Sketch of the DIT experimental setup, from Richter et al. (2016).
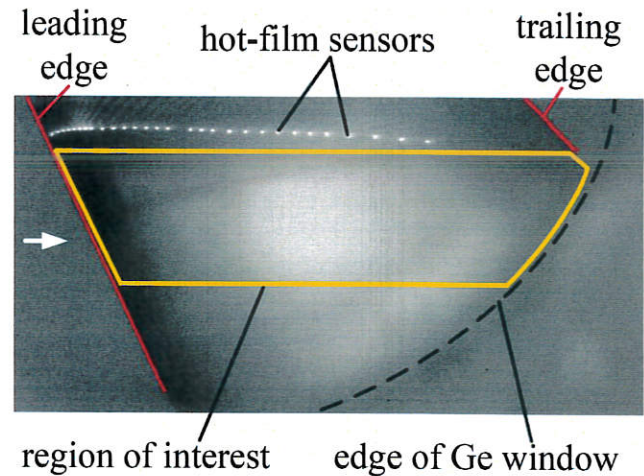

Fig. 3 Example image acquired using the setup in Fig. 2, from Raffel et al. (2015).

- A DIT image is formed by subtracting Image 2-Image 1, taken at times t_2 and t_1
- The lag of the temperature with respect to C_f is small.
- The end of the boundary layer transition region at t_1 is the downstream end of the peak
- The start of the boundary layer transition region at t_2 is the upstream end of the peak

This logic was followed by the same authors in a further paper (Raffel et al., 2015), where the start and end of boundary layer transition were found for a pitching airfoil and for a rotor with high cyclic pitch. In contrast to the theory, the experimental analyses detected the start and end of boundary layer transition at 80% of the peak height (rather than 0% as expected). This change was necessitated to avoid experimental noise, but was not theoretically supported. Richter et al. (2016) showed by a comparison of hot-film, σC_P and DIT measurements that measuring the position of the peak
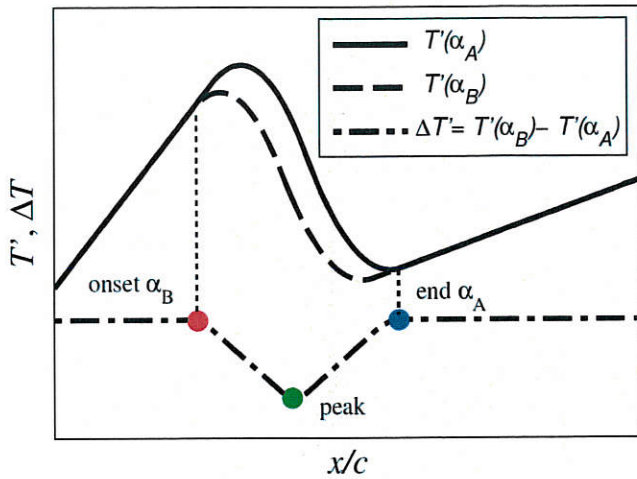
Fig. 4 Original concept diagram of the operating principle of DIT, from Raffel et al. (2015).

Fig. 5 Sketch of the numerical scheme. Heat input at the surface is by radiation, and output is by convection to the flow at the surface. At the rear wall an adiabatic condition is held. The heat is only propagated in vertical stacks.

in ΔT resulted in a boundary layer transition position at $t = (t_2 + t_1)/2$ which was comparable to boundary layer transition measurements by the other methods. The results of (Richter et al., 2016) were:

- The peak ΔT is relatively easy to detect, except where the boundary layer transition reverses direction
- The temperature lags C_f measurably
- This leads to a different shape of the temperature peak than expected for ΔC_f
- The temperature lag is visible as a changing temperature while the boundary layer transition position is stationary. this leads to potential systematic errors around the region of boundary layer transition reversal.
- The temperature peak lags other methods of boundary layer transition detection, but the difference is within the experimental uncertainty ($\Delta x/c = \pm 0.05$), and is certainly acceptable for a contactless measurement technique.

The earlier purely experimental work has noted a phenomenological correlation between the peak of ΔT and boundary layer transition position, and this paper models the experiments numerically to explain the boundary layer transition phenomena noted.

4 Theory

A code was built to compute the surface temperature using the bulk properties of the surface and time-resolved C_f and C_P distributions as input. The surface temperature was computed using the assumption of 1D heat transfer, where heat is transported in the vertical direction only. The wall is discretised by cells in the depth, and the top cell has three inputs, as illustrated in Fig. 5:

- $\dot{q} = a_d(T_r - T)$ describes the heat flux via convection to the flow from the heated wall per unit area.
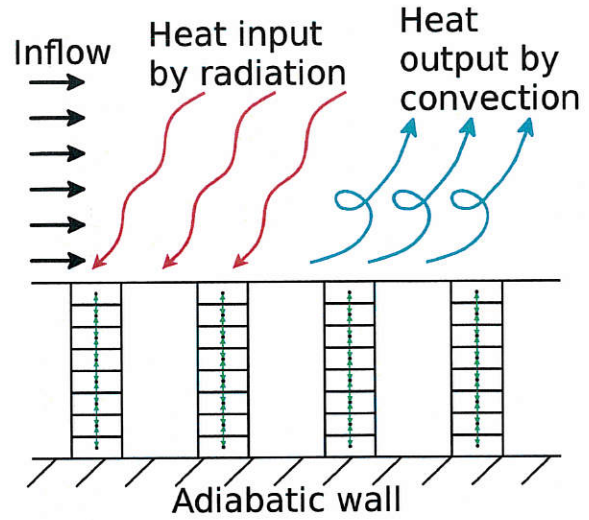
- The lamp heat flux H_L is a constant positive heat flux per unit area which is added to the surface at each time step.
- The heat flux between cells vertically is described by $\frac{\partial T}{\partial t} = a_d \frac{\partial}{\partial z}\left(\frac{\partial T}{\partial z}\right)$

The airfoil is then solved using a first order finite-difference scheme. The following assumptions and simplifications are used:

- The airfoil is infinite in the y-direction (breadth)
- The recovery temperature T_r is computed using a constant recovery factor of 0.9, independent of whether the flow is laminar or turbulent.
- The thermal diffusivity, a_d is set using the Reynolds analogy to be $a_d = 0.5 C_f \rho v C_{air}$.
- The wall does not lose any energy by radiation.
- The wall thermal properties are homogeneous.

As an output, the temperature distribution on the wall is computed as a function of time. The temperature differences are computed using a timestep equal to that from the experiment (Data taken at 190 Hz). The input time-resolved C_f and C_P distributions are computed using the DLR-TAU URANS code (Schwamborn et al., 2008). Figure 6 shows C_f, C_P and temperature distributions on the suction side of the airfoil for the same instant. After the suction peak, C_P (plotted in reversed axes) increases toward the airfoil trailing edge. The skin friction coefficient, C_f, also falls, but has a rise around x/c=0.15, associated with the boundary layer transition. The surface temperature increases toward the trailing edge, and the temperature in the middle of the airfoil of 307 K is consistent with the 306 K estimated from the infrared measurements. At the airfoil leading edge the surface temperature is approximately the same as the freestream stagnation temperature of 300 K.
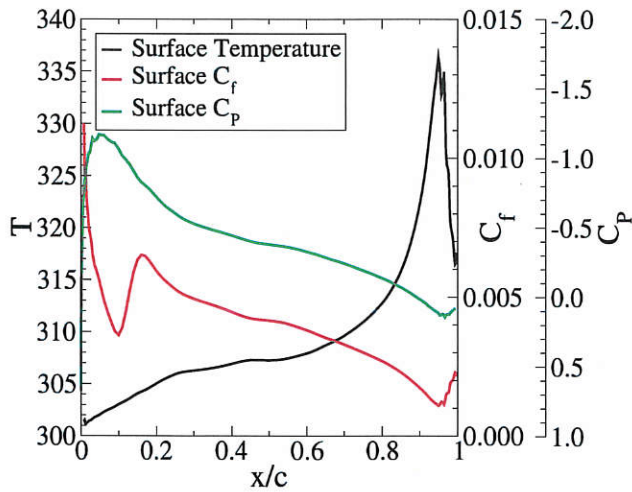
Fig. 6 Example distributions of Temperature, C_f and C_P.

Fig. 7 Time convergence of the average wall temperature.

Table 1 Numerical settings.

Cells in vertical direction	800
Cells in horizontal direction	140
Thickness of wall	5.5 mm
Time step for heat computation	5×10^{-5} s
Time step from CFD	1.5×10^{-4} s
Total time of computation	1000 s
Wall material	Epoxy
kv	0.5 W/m/K
C	2300 J/kg/K
ρ	1180 kg/m^3
Lamp heat flux H_L	2000 W/m^2
Freestream static temperature	294 K
Freestream total temperature	300 K
n-factor	10

Fig. 8 Time step convergence effect on ΔT. A time step of 5×10^{-5} s was used for computations shown in this article.

The settings for the computations are shown in Tab. 1. The bulk coefficients for epoxy were used. The spatial and time-stepping discretisation of the wall was investigated. As shown in Fig. 7, the mean temperature of the wall took 1000 s to converge, thus all computations in this paper were run for a time of 1000 s. The convergence of the wall temperature was not monitored during the experiments, but about 5 minutes of warm-up time was allowed before the first measurement. The computations on the wall are discretised in time using a time-step of 5×10^{-5} s, and the time-step of the aerodynamic data was 1.5×10^{-4} s, thus three heat-propagation time steps are taken for each aerodynamic time-step. The aerodynamic data is interpolated in time for the intermediate time-steps. The time-stepping convergence was investigated, as shown in Fig. 8, showing that all time step sizes smaller than the aerodynamic time step were equivalent. Eder (2016) suggests that for static computations where the flow does not change, that a time step of 3×10^{-2} s is sufficient. Thus the only requirement for the time step size is that the aerodynamic solution (time step 1.5×10^{-4} s) is transmitted to the surface c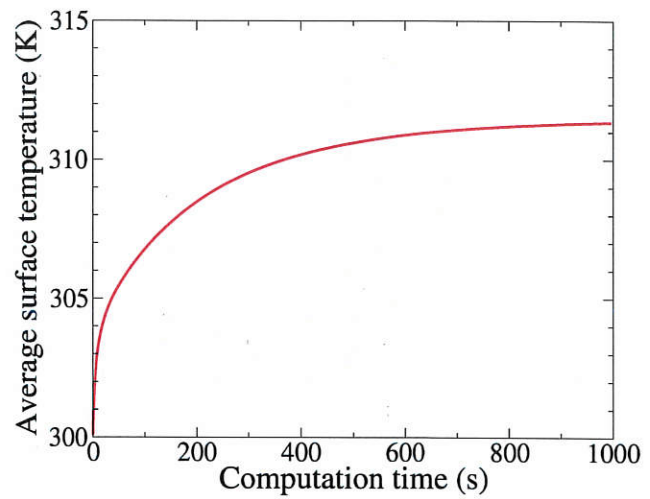ells. The grid-convergence in the vertical direction was investigated, as shown in Fig. 9. It could be shown that a grid size of 800 cells per vertical stack (cells of 6.8 μm) is sufficient to discretise the heat flux.

5 CFD computations of the skin friction and pressure coefficients

Computations were performed to produce wall skin friction coefficient C_f and wall pressure coefficient C_P data to produce synthetic data to use as an input for the computations. Since the skin friction data from the experiment was not available, a skin friction distribution as close as possible to that of the experiment was produced using a RANS solver. Although the attempt was made to closely reproduce the experimental condition, all of the conclusions of this paper are made solely using the CFD results, so any differences will be incidental.
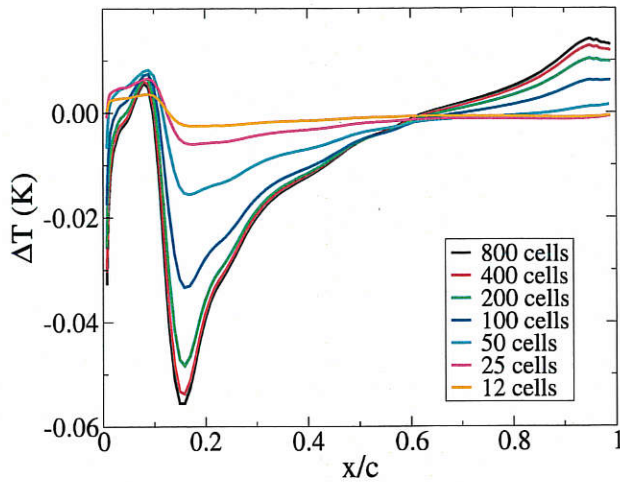
Fig. 9 Grid convergence effect on ΔT. 800 cells was used for computations shown in this article.

Fig. 10 Comparison between the experiment and CFD.

The TAU unstructured flow solver (Schwamborn et al., 2008) was used on a 2D unstructured hybrid grid generated using the Centaur® grid generator. The surface of the airfoil was resolved with cells of maximum size 1% chord, reducing to 0.1% chord at the leading and trailing edges. The boundary layer was resolved using 60 layers, using the guidelines given by Richter et al. (2011) and Krumbein et al. (2009a), and the boundary layer transition was computed using the 2D e^N transition code LILO (Schrauf, 2006) coupled with the boundary layer code COCO (COCO, 1998). The computations were performed using the Spalart-Allmaras turbulence model (Spalart and Allmaras, 1992) and the boundary layer transition was performed by switching on the turbulence production terms in the boundary layer at the "transition point", as described in detail by Krumbein et al. (2009a) and Krumbein et al. (2009b). The unsteady computations used 1024 time steps per iteration with 800 inner iterations with a 4w multigrid acceleration. The computation used a second-order time discretisation and a central second order spatial scheme. The computations were run for three cycles, of which the last two cycles were periodic. The C_f and C_P data for the last cycle was written at each time step and made available for the surface temperature code.

Figure 10 shows a comparison between the experimental and CFD movement and boundary layer transition positions, with the experimental position extracted using the σC_P method (Gardner and Richter, 2015). The CFD used a wind tunnel correction of the mean angle so that $\alpha = 4.3 \pm 6°$ is computed rather than $\alpha = 5 \pm 6°$ for the experiments. In both cases the Mach number was $M=0.3$ and the chord Reynolds number was 1.8×10^6. As detailed in AGARDograph 793 (Saric et al., 1994), the accepted selection metho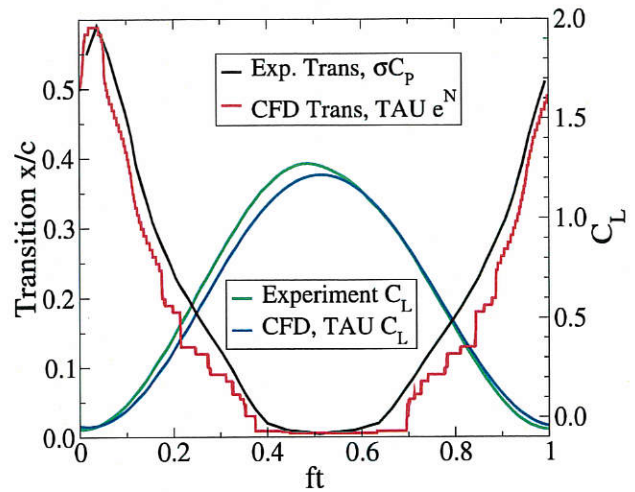d for n-factor is to use the method of Mack (1977), combined with a measurement of the turbulence level in the wind tunnel, with Eqn. 1.

$$n = -8.43 - 2.4 ln(Tu) \qquad (1)$$

From turbulence measurements in the TWG wind tunnel, the freestream turbulence level is 0.05%, and thus the N-factor used was 10. The comparison between the experiment and CFD is close enough that a qualitative similarity should be achieved, and the experiments can be used to calibrate the simulations. The boundary layer transition position in the CFD does not move smoothly, since each cell on the airfoil surface is constrained to be either laminar or turbulent, and this leads to steps in the transition position.

As shown in Fig. 11, the experimental and numerical data for the temperature difference, ΔT, agree well in amplitude, but the downstream part of the temperature difference has a different shape in the experiments than in the computations. The peak positions agree well, and the agreement is sufficient to validate the numerical approach.

6 Effect of the finite temperature delay

Boundary layer transition causes a sudden increase in the skin friction, which is associated with a change in surface heat transfer. The distribution of C_f for boundary layer transition with the airfoil pitching up and transition on the suction side moving towards the leading edge with advancing time is shown at three different times in Fig. 12, along with the difference in C_f. It can be noted that these computed values agree well with the concept sketch of Raffel et al. (2015) shown in Fig. 4. Raffel et al. posited that the start and end of boundary layer transition are visible as the start and end of the C_f peak, and this is true, although the exact definition of the peak ends is difficult. Note particularly that a visible difference between the two C_f distributions continued down-
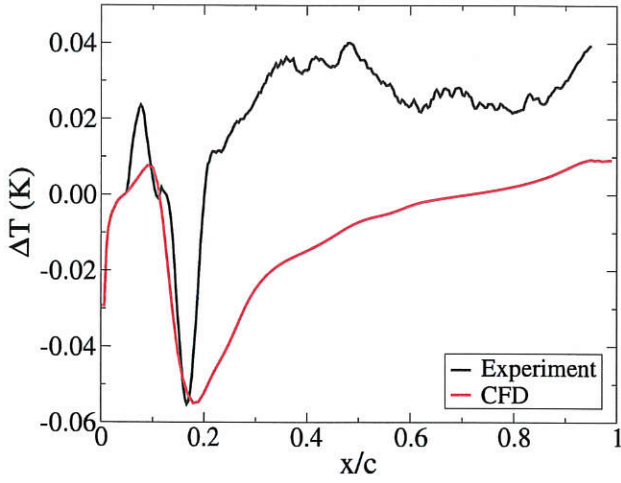
Fig. 11 Comparison between Experiment and CFD temperature distributions at $\alpha=3.25°$ on the upstroke.
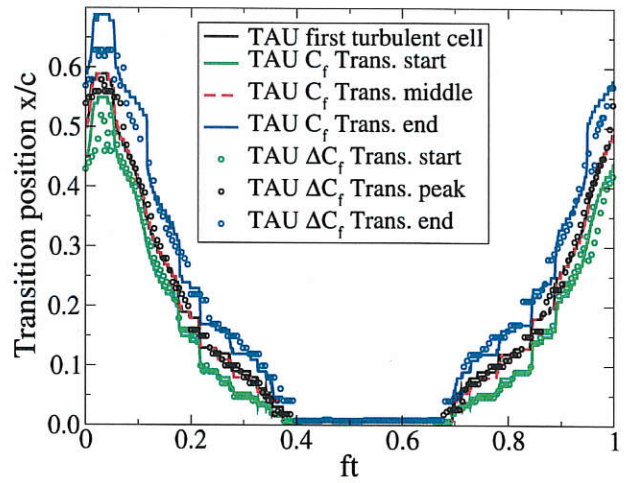

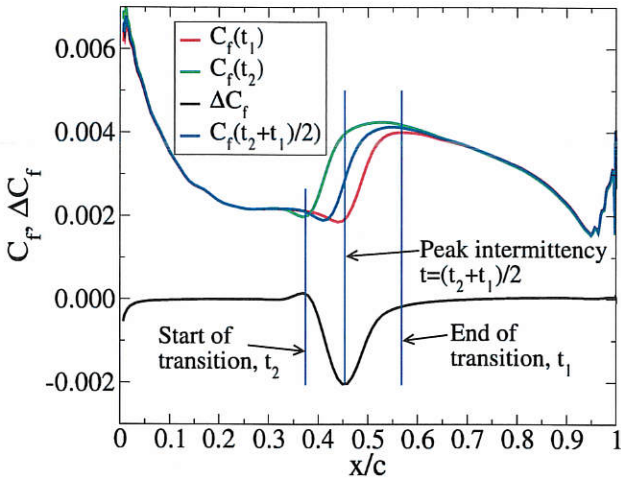**Fig. 13** Comparison of boundary layer transition points from the computations.

Fig. 12 For the dynamically pitching airfoil the difference image ΔC_f is produced using a difference between the C_f distributions at times t_1 and t_2, with the airfoil pitching up and boundary layer transition on the suction side moving towards the leading edge with advancing time.

stream of the end of transition for t_1. Perhaps more practically, Richter et al posited that the peak in ΔC_f corresponds to the boundary layer transition position at $t = (t_2 + t_1)/2$. Although there is no particular reason why this must be the case, it appears to be true for the cases investigated in this paper.

The definition of a boundary layer transition point as applied to CFD can be at variance to the experimentally applied maximum intermittency or maximum gradient in C_f. Figure 13 shows a comparison between different computations of the transition points from computational data. The official boundary layer transition point from the computation is the point at which the turbulence production is switched on, as noted by the black line. This correlates very well with the boundary layer transition point computed as

the point of maximum gradient in the C_f curves (intermittency is not available in the computations). The turbulence production has an upstream effect and the start of boundary layer transition can be noted as the point where the gradient of C_f passes zero, and the downstream end is where the gradient in boundary layer transition passes zero on the downstream side. Analysing the difference curves, the peak in ΔC_f fits well to the boundary layer transition position from the solver and that from the C_f maximum gradient well. The upstream and downstream ends of the boundary layer transition region are determined as the points of zero gradient in the C_f curve. If these are compared with the start and end of the ΔC_f peak, detected as peaks in the second derivative of the ΔC_f curve, the agreement is relatively good, even considering problem areas as near $ft=0.7$ where the automated detection cannot detect the second derivative correctly. Using the second derivative in ΔC_f to detect the start and end of the peak is not physically based, but serves as a replacement for the sharp start and end of the curve, as postulated in Fig. 4.

The above shows that the basic idea of Raffel and Merz (2014) is correct, however the C_f distribution is not directly measured using IR thermography, rather the temperature distribution is measured. Figure 14 shows a comparison between temperature ΔT and skin friction ΔC_f differences at an acquisition rate of 190 Hz on the upstroke. Figure 15 shows the same figure for the downstroke. The ΔT are negative when the ΔC_f peaks are positive (and the opposite), since increased C_f increased the cooling of the airfoil and reduces the temperature. The ΔT peak positions always lag the ΔC_f peak positions in time, and the shape of the ΔT peaks is different than the ΔC_f peaks, with the ΔT peaks having a sharp edge in the direction of travel and a long tail in the opposite direction. Thus in the downstroke, the downstream edges of the peak are sharp and the upstream edges
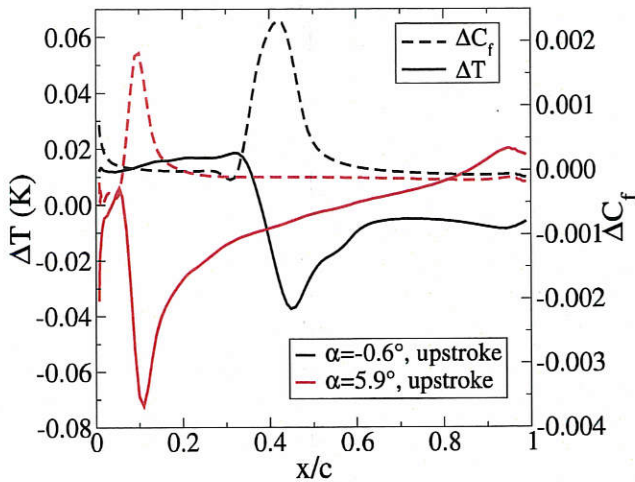
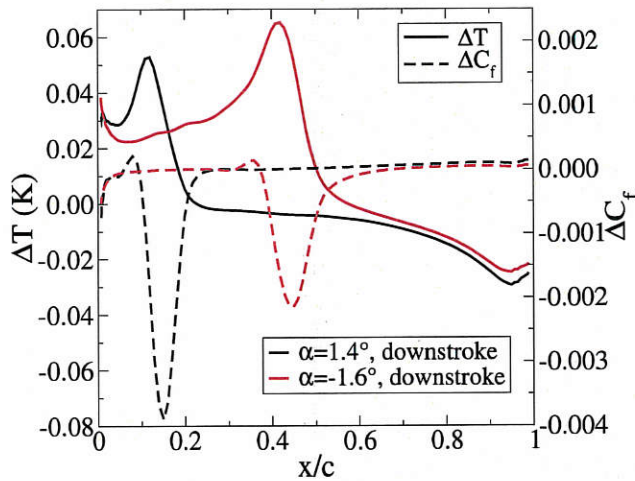**Fig. 14** Comparison of ΔT and ΔC_f distributions during the upstroke.

Fig. 15 Comparison of ΔT and ΔC_f distributions during the downstroke.

Fig. 16 For the same case as Fig. 13, the boundary layer transition position as given by the peak of temperature.

are blurred, and the upstream edge is sharp on the upstroke. With changing angle of attack, the position of the stagnation point on the airfoil changes significantly, and this results in a change in the wetted length of the airfoil (by about x/c=0.1). Additionally, the Mach number and local density of the flow over the airfoil change depending on the angle of attack. The result is that all positions on the airfoil have a sinusoidal temperature change during a pitching cycle, and this is visible in the ΔT positions outside the peak positions. The width of the ΔT peak increases with increasing length of the boundary layer transition region, but the start and end of the transition region cannot be extracted as a feature from the ΔT distribution.

The peak of the ΔT distribution was extracted and plotted in Fig. 16. The cyan crosses are the most reliable method of boundary layer transition position detection and are extracted by selecting the minimum of ΔT on the upstroke and
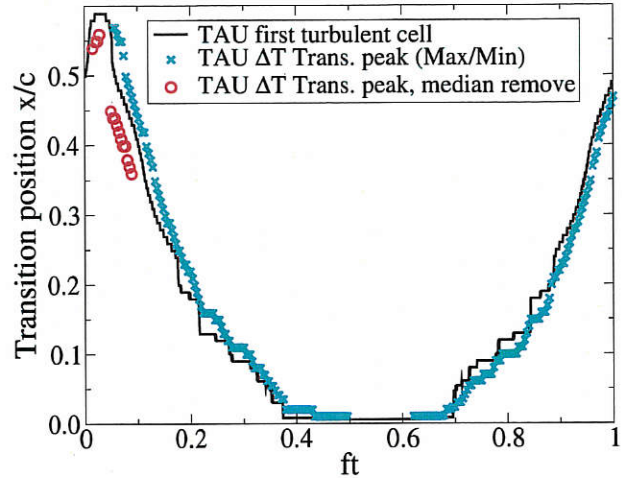
the maximum of ΔT on the downstroke, switching when the physical direction of airfoil pitching changed. A systematic error is introduced due to the time lag of ΔT behind ΔC_f, but this is constrained to 1.5 ms, or an error in the transition position of x/c=0.05. The 1.5 ms delay is uniform over the whole pitching cycle, independent of pitching rate $\dot{\alpha}$ or boundary layer transition position. An alternative method of boundary layer transition position detection was used by Richter et al. (2016) and compares the absolute sizes of the positive and negative ΔT peaks when the median of the whole ΔT distribution is subtracted. This method is more generalisable, since it does not rely on *a priori* knowledge of the direction of boundary layer transition movement, and at most points the same result is achieved as simply using the maxima of ΔT. At the red circles in Fig. 16, a different transition position is systematically predicted. This is related to the problem of detection of the boundary layer transition position when the transition position is momentarily unmoving. Fig. 17 shows the analysis from Richter et al. (2016), showing the experimentally detected points for boundary layer transition using DIT. At the upstream-most point of boundary layer transition no transition point could be found, but the static IR images could be analysed to give a boundary layer transition position. At the downstream-most point of boundary layer transition the detected transition has a systematic error, and the static IR data was not usable due to the low local wall shear stress.

Figure 18 shows ΔT distributions around the downstream point where the boundary layer transition direction changes, from downstream movement to upstream movement. It can be seen that at the moment of reversal ($ft=0$), where the boundary layer transition position movement is zero, a strong positive peak in ΔT is visible. This is different to the prediction of Raffel and Merz (2014), who would have expected zero signal at this position. After this time, the positive peak
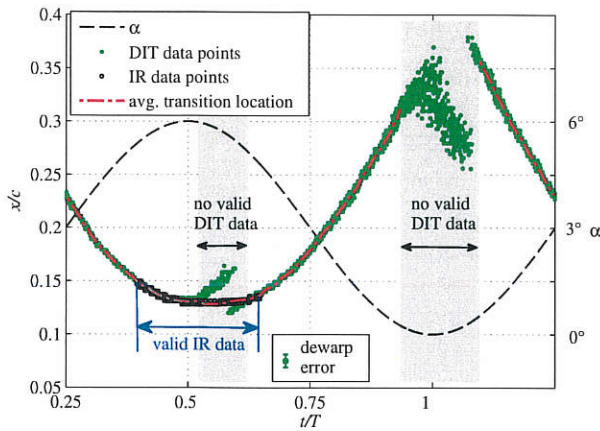
Fig. 17 Figure from Richter et al. (2016), showing the experimentally detected points for boundary layer transition using DIT. The systematic error is due to the use of max(abs(ΔT_{min}-ΔT_{median}), abs(ΔT_{max}-ΔT_{median})) as the detection criterion for the transition point. The alternative is to always use ΔT_{min} on the upstroke and ΔT_{max} on the downstroke, switching as the movement of the airfoil switches. The difference between these two approaches can be seen in Fig. 16.

Fig. 18 Illustration of the problem with peak detection at the point of reversal in the direction of travel of the boundary layer transition position. Due to the delay of the temperature distribution behind the C_f distribution, an incorrect peak is produced, which moves upstream on the airfoil.

in ΔT rapidly reduces, and the new negative peak in ΔT caused by the upstream movement of the boundary layer transition position is superimposed on the old ΔT distribution. By $ft=0.036$, the negative temperature peak is visible, and the transition is moving upstream with the ΔT peak position slightly lagging the true transition position. In the change between the positive and negative ΔT peaks, there is a region where both a positive and a negative peak are visible. The positive peak is not associated with the boundary layer transition position, and a detection algorithm which follows this peak leads to a detection of the transition position rapidly moving upstream (see the black dotted line), whereas in reality it is nearly stationary. Adding knowledge about the direction of boundary layer transition travel means that up to $ft=0$ ΔT_{max} is detected, and thereafter ΔT_{min}. This means that the false peak is not detected, but that at times less that $ft=0.021$ no valid negative peak can be found, and thus boundary layer transition cannot be detected using DIT.

7 Effect of material selection

The selection of an appropriate surface material obviously has an effect on the surface temperature distribution response to dynamically changing flows. Simon et al. (2016), noted that the temperature change increased by a factor of 1.8 when the aluminium sheets used were painted. Generally, lower heat capacity materials and and better thermal insulators should give a larger signal. To investigate this effect, the surface temperature was computed for the range of material constants in Table 2. Particularly materials 3-7 represent machinable materials which could reasonably be used for a
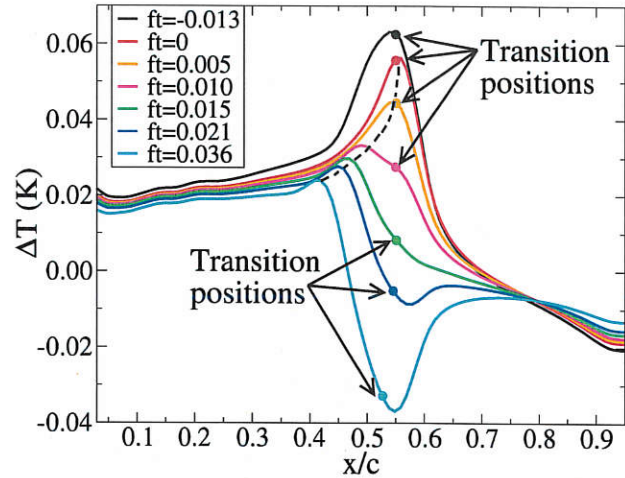
Table 2 Example materials.

Ref. #	kv	C_p	ρ (kg/m³)	Example material
1	0.05	1300	20	expanded polystyrene
2	0.05	1900	250	cork
3	0.1	1300	1100	polystyrene
4	0.15	1400	1100	Mylar®
5	0.2	1500	1200	Plexiglass®
6	0.3	2300	1200	polyethelyne
7	0.5	2300	1180	epoxy
8	0.6	2800	2200	Pyrex® glass

wind tunnel model, either as full material, or as a surface covering with a foil or contact sheet. Table 2 lists approximate bulk material constants, and it is questionable whether for materials 1 and 2, expended polystyrene or cork have these properties on a small scale.

The material selection can effect both the size of the ΔT peak signal and the time delay between the peak position and the position of boundary layer transition. The peak height is compared for the different materials in Fig. 19. With the exception of materials 1 and 2, the variation in signal strength is limited to a factor of three compared to epoxy. Interesting to note is that epoxy is one of the worst materials in terms of signal strength. In contrast to these results, the effect of different materials on the time delay between the ΔT peak and the true boundary layer transition position is negligible. Figure 20 shows that for materials 2-8 the time delay between the ΔT peak and the true boundary layer transition position is 1.4-1.5 ms, and for material 2 it is 1.3 ms. Although generally better thermal insulators had a faster response, the effect is not significant except for material 1. The importance of the small-scale material properties (as opposed to bulk properties) is made clear in Fig. 21. Here the variation in
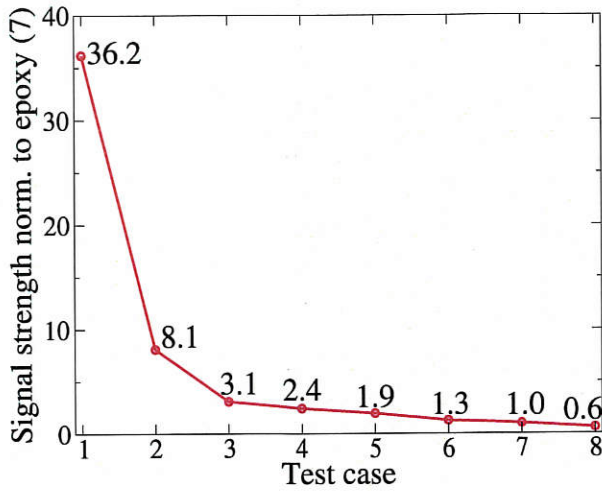
Fig. 19 Comparison of the signal strength in the temperature difference images for the materials in Table 2. The results are consistent with the order of the effects noted by Simon et al. (2016).

Fig. 21 Variation of temperature in a single stack of cells near the airfoil leading edge over a pitching cycle for material 7 (Epoxy).
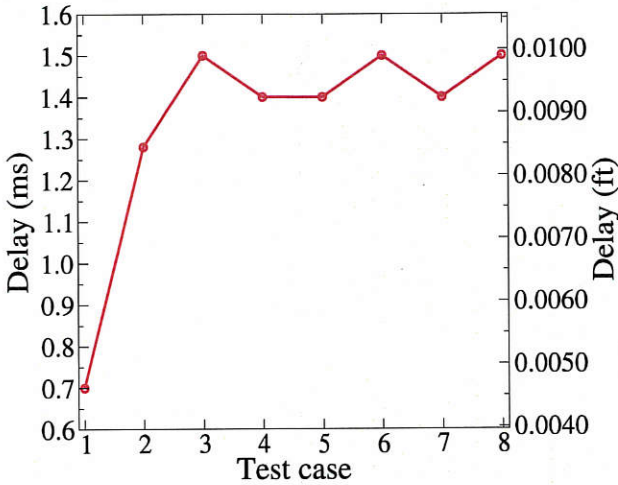

Fig. 20 Comparison of the time delay in the detected boundary layer transition position compared to the true transition position for the materials in Table 2.

temperature over the thickness of the surface is plotted for epoxy, for a cell at x/c=0.56. It can be seen that the variation is restricted to the first 0.5 mm, with the majority of the variation in the first 0.1 mm. Generally the heat conduction is a small-scale phenomenon, and any large-scale heat conduction occurs on much longer time-scales than those of the unsteady flow, as also indicated by the heating time curve in Fig. 7. This investigation indicates that the use of paint or contact sheets with a thickness of 100-200 μm is probably sufficient to control the surface properties.

8 Conclusions

An analysis of Differential Infrared Thermography (DIT) for the detection of dynamically moving boundary layer tran-
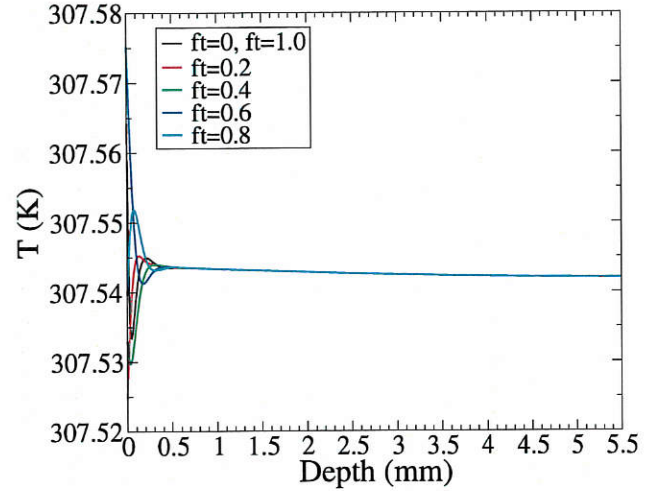
sition positions has been performed for a pitching airfoil with Mach 0.3, Reynolds number 1.8×10^6 with sinusoidal pitching at $\alpha = 5 \pm 6°$. The surface temperature was computed using a finite difference method, and flow input from CFD. The temperature differences, ΔT, were generated to match the experimental camera frame rate of 190 Hz. The important results were:

- The assertion of Richter et al. (2016) that the ΔT peak indicates the boundary layer transition position is confirmed.
- The ΔT peak lags the true boundary layer transition position by about 1.5 ms, and this lag is insensitive to the selection of the surface material.
- The dynamic temperature variation detected by DIT only affects the top 0.5 mm of the surface, with the main variation much closer to the surface. Thus the use of paint or contact sheets with a thickness of 100-200 μm is probably sufficient to control the surface properties. The ΔT peak signal can be improved by a factor of three by the selection of appropriate surface materials.
- When the boundary layer transition position is moving, the detection of the ΔT peak is insensitive to the method used. When the direction of movement of the boundary layer transition direction reverses, the detection of the ΔT peak position is difficult, and some algorithms result in a systematic error in the boundary layer transition position.
- Contrary to the original assertions of Raffel and Merz (2014), the start and end of the peak in ΔT are not correlated with a particular position in the boundary layer transition process. Despite this, a wider peak indicates a longer boundary layer transition length.

The usefulness of DIT for the detection of dynamic stall is confirmed, and the accuracy is acceptable for a non-contact

optical method which is capable of detecting 3D boundary layer transition positions.

References

Astarita, T., Cardone, G., (2000) Thermofluidynamic analysis of the flow in a sharp 180 degrees turn channel. In: Experimental Thermal and Fluid Science, Vol. 20, No. 3-4, pp188-200

Bouchardy, A.-M., Durand, G., Gauffre, G., (1983) Processing of Infrared Thermal Images for Aerodynamic Research. In: Applications of Digital Image Processing, Vol. 397, pp. 304-309.

Carlomagno, G. M., Cardone, G., (2010) Infrared thermography for convective heat transfer measurements. In: Experiments in Fluids, Vol. 49, No. 6, pp. 1187-1218

COCO: A Program to Compute Velocity and Temperature Profiles for Local and Nonlocal Stability Analysis of Compressible, Conical Boundary Layers with Suction, In: Center of Applied Space Technology and Microgravity Technical Rept., Nov. 1998.

Døssing, M. (2008) High frequency microphone measurements for transition detection on airfoils. Risø-R-1645(EN)

Du, Z., Selig, M. S. (2000). The effect of rotation on the boundary layer of a wind turbine blade. Renewable Energy, 20(2), 167-181.

Eder, C., (2016) Analyse der Differenzinfrarotthermographie (Engl: Analysis of Differential Infrared Thermography), Masters Thesis, University of the Bundeswehr, Munich, August 2016.

Gardner, A.D., Richter, K., (2015) Boundary layer transition determination for periodic and static flows using phase-averaged pressure data. In: Experiments in Fluids, Vol. 56, No. 6. DOI: 10.1007/s00348-015-1992-9

Gardner, A. D., Wolf, C.C., Raffel, M., (2016) A new method of dynamic and static stall detection using infrared thermography, In: Experiments in Fluids, Vol. 57, No. 9, 2016. DOI: 10.1007/s00348-016-2235-4

Gartenberg, E., Roberts, A.S. Jr. (1992) Twenty-Five Years of Aerodynamic Research with Infrared Imaging. In: Journal of Aircraft, Vol. 29, No. 2, pp161-171.

Heister, C.C. (2013) Numerical Investigation of Laminar-Turbulent Transition Mechanisms for Helicopter Rotors in Forward Flight, In: American Helicopter Society 69th Annual Forum, Phoenix, Arizona, May 21-23, 2013.

Krumbein, A., Krimmelbein, N., Schrauf, G. (2009a) Automatic Transition Prediction in Hybrid Flow Solver, Part 1: Methodology and Sensitivities, In: Journal of Aircraft, Vol. 46, No. 4, DOI: 10.2514/1.39736

Krumbein, A., Krimmelbein, N., Schrauf, G. (2009b) Automatic Transition Prediction in Hybrid Flow Solver, Part 2: Practical Application", Journal of Aircraft, Vol. 46, No. 4 DOI: 10.2514/1.39738

Langtry, R., Gola, J., Menter, F. (2006). Predicting 2D airfoil and 3D wind turbine rotor performance using a transition model for general CFD codes. In 44th AIAA aerospace sciences meeting and exhibit (p. 395).

Lanzafame, R., Mauro, S., Messina, M. (2013). Wind turbine CFD modeling using a correlation-based transitional model. Renewable Energy, 52, 31-39.

Mack L.M., *Transition prediction and linear stability theory*, AGARD Conf. Proc. no 224, Paris, 1977 - Also JPL Publication 77-15, 1977

Nitsche, W., Brunn, A. (2006) Strömungsmesstechnik. (Engl. Flow measurement techniques). Springer, ISBN: 978-3540209904

Quast, A., (1987) Detection of Transition by Infrared Image Technique. In: 12th international congress on instrumentation in aerospace simulation facilities (ICIASF 87), Williamsburg, VA, 22-25 June 1987, pp. 125-134

Richards, E. J., Burstall, F.H., (1945) The "China Clay" method of indicating transition. ARC R&M, No. 2126, HM Stationery Office, August 19 1945.

Richter, K., Le Pape, A., Knopp, T., Costes, M., Gleize, V., Gardner, A.D., (2011) Improved Two-Dimensional Dynamic Stall Prediction with Structured and Hybrid Numerical Methods, In: Journal of the American Helicopter Society, Volume 56, Issue 4. doi:10.4050/JAHS.56.042007

Richter, K., Schülein, S., (2014) Boundary-layer transition measurements on hovering helicopter rotors by infrared thermography. In: Experiments in Fluids, Vol. 55, No. 7. DOI: 10.1007/s00348-014-1755-z

Richter, K., Wolf, C.C., Gardner, A.D., Merz, C.B, (2016) Detection of Unsteady Boundary Layer Transition Using Three Experimental Methods. In: 54th AIAA Aerospace Sciences Meeting, San Diego (CA), USA, 4-8 January 2016, AIAA-2016-1072

Raffel, M., de Gregorio, F., de Groot, K., Schneider, O., Gibertini, G., Seraudie, A., (2011) On the Generation of a Helicopter Aerodynamic Database, In: Aeronautical Journal, Vol. 115, No. 1164, 2011, pp. 103-112 doi:10.2514/1.J053235

Raffel, M., Merz, C.B. (2014) Differential Infrared Thermography for Unsteady Boundary-Layer Transition Measurements, In: AIAA Journal, Vol. 52, No. 9, 2014. pp. 2090-2093. DOI: 10.2514/1.J053235

Raffel, M., Merz, C.B, Schwermer, T., Richter, K., (2015) Differential infrared thermography for boundary layer transition detection on pitching rotor blade models. In: Experiments in Fluids, Vol. 56, No., 2, DOI 10.1007/s00348-015-1905-y

Saric et al., *Progress in Transition Modelling*, AGARD-R-793; 1994.

Schrauf, G., (2006) LILO 2.1 User's Guide and Tutorial, Geza Schrauf Stability Computations Tech. Rept. 6, originally issued Sept. 2004, modified for Ver. 2.1 July 2006.

Schülein, E. (2014) Optical method for skin-friction measurements on fast-rotating blades. Exp Fluids doi:10.1007/s00348-014-1672-1

Schultz, D.L., Jones, T.V. (1973) Heat-transfer measurements in short-duration hypersonic facilities. AGARDograph 165.

Schwamborn, D., Gardner, A. D., von Geyr, H., Krumbein, A., Lüdeke, H., and Stürmer, A., (2008) Development of the TAU-Code for Aerospace Applications, In: 50th NAL INCAST (International Conference on Aerospace Science and Technology), Bangalore, India, June 26-28, 2008.

Simon, B., Filius, A., Tropea, C., Grundmann, S., (2016) IR thermography for dynamic detection of laminar-turbulent transition. In: Experiments in Fluids, Vol. 57, No. 5. DOI: 10.1007/s00348-016-2178-9

Spalart, P. R., and Allmaras, S. R., (1992) A One-Equation Turbulence Model for Aerodynamic Flows, AIAA 1992-0439, In: AIAA 30th Aerospace Sciences Meeting and Exhibit, Reno, NV, January 6-9, 1992

Thomann, H., and Frisk, B., (1967) Measurement of Heat Transfer with an Infrared Camera. In: International Journal of Heat and Mass Transfer, Vol. 11, pp. 819-826.

Uenal, E., and Grieb, H., (2013 Stall and Transition on Elastic Rotor Blades T1.1 DSA-9A Static Validation of Wind Tunnel Model. Ferchau Engineering Report, 2013.

Velkoff, H.R., Blaser, D.A., Jones, K.M. (1971) Boundary-layer discontinuity on a helicopter rotor blade in hovering. J Aircraft, Vol. 8, No. 2, pp. 101-107. doi:10.2514/3.4423610.2514/3.45910